The International Journal of Advanced Manufacturing Technology (2019) 103:1419–1431
https://doi.org/10.1007/s00170-019-03616-2

ORIGINAL ARTICLE

Analysis and constitutive modelling of high strain rate deformation behaviour of wire–arc additive-manufactured ATI 718Plus superalloy

G. Asala[1] · J. Andersson[2] · O. A. Ojo[1]

Received: 31 January 2019 / Accepted: 18 March 2019 / Published online: 5 April 2019

Abstract
A fundamental prerequisite for obtaining realistic finite element simulation of machining processes, which has become a key machinability assessment for metals and alloys, is the establishment of a reliable material model. To obtain the constitutive model for wire–arc additive-manufactured ATI 718Plus, Hopkinson pressure bar is used to characterise the flow stress of the alloy over a wide range of temperatures and strain rates. Experiment results show that the deformation behaviours of as-deposited ATI 718Plus superalloy are influenced by the applied strain rate, test temperature and strain. Post-deformation microstructures show localised deformation within the deposit, which is attributable to the heterogeneous distribution of the strengthening precipitates in as-deposited ATI 718Plus. Furthermore, cracks are observed to be preferentially initiated at the brittle eutectic solidification constituents within the localised band. Constitutive models, based on the strain-compensated Arrhenius-type model and the modified Johnson–Cook model, are developed for the deposit based on experimental data. Standard statistical parameters, correlation coefficient (*R*), root-mean-square error (*RMSE*) and average absolute relative error (*AARE*) are used to assess the reliability of the models. The results show that the modified Johnson–Cook model has better reliability in predicting the dynamic flow stress of wire–arc-deposited ATI 718Plus superalloy.

Keywords Additive manufacturing · High strain rates · Machining · Ni-based superalloys · Constitutive modelling · Johnson–Cook

1 Introduction

ATI 718Plus is a Ni-based superalloy, developed in a bid to improve the service temperature of the extensively used Ni–Fe-based superalloy, IN 718, for aerospace applications to enhance its efficiency [1]. This relatively new alloy has demonstrated about 50 °C increase in the service temperature above what is usually required for Alloy 718, while still maintaining its desirable processability. It is bid to serve as a higher temperature substitute for Alloy 718 and to help reduce the cost of employing other more expensive higher temperature alternatives in aerospace applications [2].

Wire–arc additive manufacturing (WAAM) is a promising high-deposition additive manufacturing (AM) process, suitable for adding structural details to simpler semi-finished parts and for the total fabrication of large metal parts with moderate complexity [3, 4]. This wire-based directed energy deposition (DED) process utilises electric arc to melt and add feedstock wire to fabricate near-net-shaped components. Follow-on machining is a crucial post-deposition part of the process required to put the tolerance and surface quality of the deposited components in order.

Machining is a high strain rate deformation process, and understanding of the complex material response during this metal removal process is vital in enhancing the machinability of the workpiece. Finite element (FE) modelling of the machining processes has been found to be a beneficial and efficient tool in evaluating the machinability of metals and alloys and the optimisation of machining process conditions while reducing the number of costly experimental trials needed [5].

✉ G. Asala
gbengaa@myumanitoba.ca

J. Andersson
joel.andersson@hv.se

O. A. Ojo
olanrewaju.ojo@umanitoba.ca

[1] Department of Mechanical Engineering, University of Manitoba, Winnipeg R3T 5V6, Canada

[2] Department of Engineering Science, University West, SE-461 86 Trollhättan, Sweden

Table 1 The composition of ATI 718Plus® filler wire

ATI 718Plus®	Element	Ni	Nb	Fe	W	Cr	Ti	Al	Mo	Co	Mn (ppm)	Si (ppm)	P (ppm)	B (ppm)
Additive wire	wt%	52.2	5.5	9.1	1.0	17.6	0.8	1.5	3.1	9.2	200	200	5	30

It is, however, worth noting that obtaining a reliable material model which describes the dynamic flow behaviour of the workpiece, comparable to those occurring during the cutting operations, is the foundation to achieving an accurate and reliable machining model [6].

Presently, there are several models used to describe the dynamic flow stress of materials under high strain rates and temperatures; the two most popular among them are the Johnson–Cook (J-C) [7] and the Arrhenius-type [8] models. The J-C model has been extensively applied in simulating machining processes and has also found application in the modelling of impact loading in structural components. The original model assumed that the influences of strain rate hardening, strain hardening and thermal softening on the flow stress of materials are mutually independent, and the coupled effects of these factors were ignored. In most materials, however, the coupled effects of temperature, strain rate and strain on the flow stress are usually observed. Owing to this deficiency, modifications to the J-C model have been made by different authors [9–15] to capture these coupled effects. Lin et al. [9] introduced some material constants to consider the coupled effects of temperature and strain rates in predicting the flow stress of high-strength steel, and the results obtained showed that the modified version significantly improves the accuracy of the predicted material behaviour.

The Arrhenius-type (AT) model is another common phenomenological-based model used to describe plastic flow behaviour of materials at high temperatures and strain rates. The AT model, proposed by Sellars and McTegart [8], has also undergone several modifications over the years, including the introduction of the Zener–Hollomon parameter (Z) [16] and a strain-dependent parameter [17, 18] to improve the predictability of the model for different materials. Recently, a compensation of strain for the material constants in the Arrhenius-type model was proposed by Lin et al. [19]. This strain-compensated Arrhenius (ATC) model has been successfully applied to predict, with improved accuracy, the flow stress of metals and alloys over a wide range of temperature and strain rates.

In using wire-based DED as a manufacturing route for ATI 718Plus components, the subsequent machining operations of the deposited part are important in the process. FE modelling can serve as a viable route to optimise the machinability of this difficult-to-cut alloy and will require a reliable material model to predict the flow stress of the deposit. There is, however, limited quantitative data of the flow behaviour of as-deposited ATI 718Plus in the open literature. This present study is aimed at obtaining the deformation behaviour of as-deposited ATI 718Plus, at different strain rates and temperature, using a Hopkinson pressure bar, and in establishing a constitutive model that can reliably predict the flow behaviour. To this end, the modified J-C model and ATC were applied to describe the flow stress of the alloy. The reliability of these two models to predict the flow stress of the deposited alloy is assessed based on the average absolute relative error (*AARE*), root-mean-square error (*RMSE*) and the correlation coefficient (R).

2 Materials and methods

2.1 Wire–arc deposition of ATI 718Plus superalloy

The chemical composition of the additive wire for deposition in the study is presented in Table 1. The diameter of the additive wire is about 1.6 mm and was deposited on the substrate plate (wrought ATI 718Plus) using a tungsten inert gas (TIG) system integrated with a 6-DOF Panasonic robot. A block of deposited material with a dimension of about 100 mm × 70 mm 20 mm, from which the deformation test specimens were extracted, was produced using the deposition parameters as stated in Table 2.

After the deposition, cylindrical specimens with dimension of 9.5 mm in diameter and height of 9.0 mm were machined along the build direction, for quasi-static and high strain rate test experiments, using electric discharge machining (EDM).

Table 2 Parameters used for wire–arc additive manufacturing of the block

Parameter for WAAM deposition	
Arc current (A)	100
Travel speed (m/min)	0.1
Wire feed rate (m/min)	0.4
Average arc length (mm)	4

2.2 High strain rate deformation of as-deposited ATI 718Plus

The quasi-static compression behaviour of the as-deposited WAAM ATI 718Plus was characterised using the United hydraulic testing machine, which has a maximum load capacity

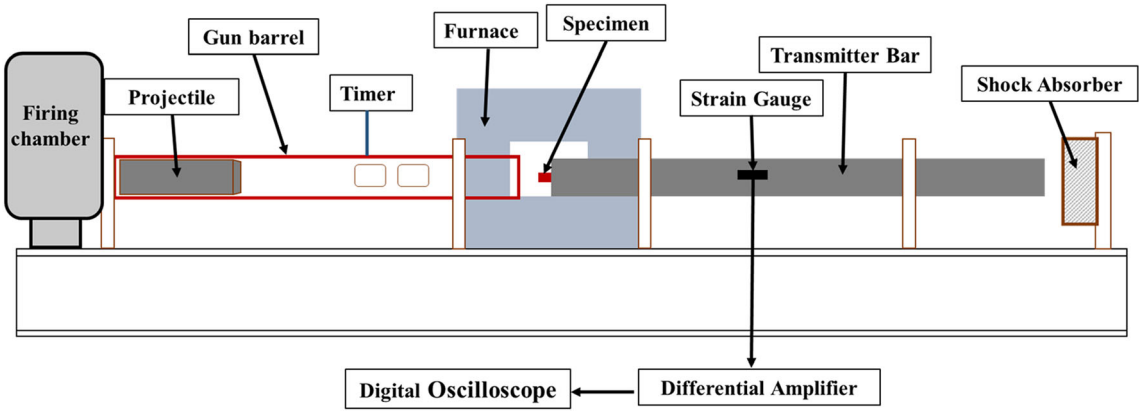

Fig. 1 A schematic diagram of a direct-impact Hopkinson bar

of 600 kN. The deformation was carried out at an approximate strain rate of 1 s^{-1}.

The dynamic flow stress of the as-deposited ATI 718Plus, at high strain rates, was characterised using a direct-impact Hopkinson pressure bar (DIHPB) system, shown schematically in Fig. 1. The length of the projectile and the transmission bar is 225 mm and 1.5 m, respectively, and the impact ends are hardened and have hardness values of approximately 53 HRC. A detailed description of the DIHPB and the method for testing can be found elsewhere [20, 21]. The surface of the samples was polished, and lubricant (molybdenum disulphide grease or graphite) was applied at the specimen–bar interface to reduce friction during the deformation test. The specimens were deformed at different impact momentum (from 20 to 35 kg m/s), translating to average strain rates between 1500 and 3500 s^{-1} as summarised in Table 3, and over a range of deformation temperatures (from 25 to 800 °C). To allow for easy specimen transfer from the furnace to the impact site in a safe and repeatable manner during the tests at high temperatures, a fixture is attached to the Hopkinson bar system. To estimate heating and cooling times during the sample transfer, a dummy specimen equipped with a thermocouple was used to monitor the heating and cooling rates. Soaking time of about 8 min was found to be acceptable for heating and homogenising the specimen at the desired test temperature. At 800 °C, the temperature drop after 10 s of removing the specimen from the furnace is estimated to be approximately 14 °C. The average time for the test specimen to leave the furnace until impact was found to be between 4 and 6 s, and the test specimen is super-heated at 10 °C above the test temperature to account for the temperature drop.

The elastic wave signals in the transmitter bar, captured and recorded by the oscilloscope, were then used to calculate the true stress–true strain data [20].

The alloys in the as-deposited condition, before and after deformation, were sectioned and mounted in a conductive Bakelite. They were then subjected to grinding and polishing using the standard metallographic techniques and electro-etched in 170 mL of phosphoric acid(H_3PO_4) + 10 mL of sulphuric acid (H_2SO_4) + 15 g of chromium trioxide (CrO_3) at 5 V for 20 s. The microstructure of the alloys was characterised using a Carl Zeiss Axio Vert-inverted optical microscope and JEOL 5900 scanning electron microscope.

3 Results and discussion

3.1 Undeformed microstructure of wire–arc-deposited ATI 718Plus

Figure 2a presents the optical micrograph of wire–arc-deposited ATI 718Plus, showing the clad tracks typical for wire-based AM. The scanning electron micrograph (SEM) of the as-deposited alloy is presented in Fig. 2b. The SEM image shows a dendritic solidification microstructure having the inter-dendritic regions laced with secondary-phase

Table 3 Impact momentum used to deform WAAM ATI 718Plus and the corresponding average strain rates at 273 K

Alloy type	Alloy condition	Impact momentum (kg m/s)	Average strain rate (s^{-1})
WAAM ATI 718Plus	As-processed	20.4	1586
		28.5	2907
		35.6	3422

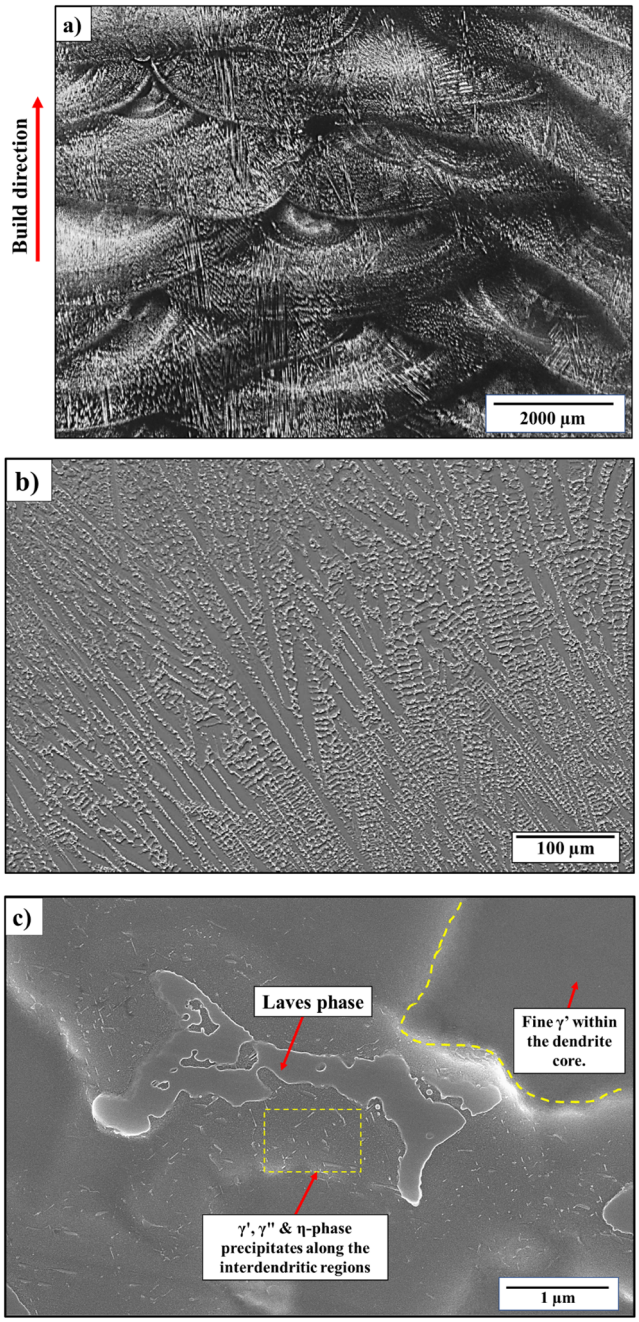

Fig. 2 (**a**) Optical micrograph of the wire–arc-deposited ATI 718Plus showing the clad track; (**b**) SEM image showing the dendritic solidification structure and eutectic constituents along the interdendritic regions; (**c**) high-magnified SEM image showing the precipitation of γ', γ'' and η-phase particles in proximity to the solidification particles

eutectic constituents. A closer magnified SEM image of the interdendritic region, in Fig. 2c, shows the precipitation of some particles close to the eutectic constituents. The morphology of the precipitates suggests them to be a combination of strengthening precipitates and the plate-like, η-phase particles. An earlier study by Asala et al. [22], detailing the microstructural evolution during wire–arc deposition of ATI 718Plus, identified the constituents as Laves phase and MC carbide particles formed due to micro-segregation during solidification. Similarly, segregation-induced inhomogeneous formation of precipitates, confirmed to be γ', γ'' and η-phase precipitates, along the interdendritic regions of the deposit, was also reported. The influence of these microstructure and post-deposition heat treatment on the mechanical properties of the deposit, in comparison with the wrought counterpart, has also been reported by Asala et al. [21].

3.2 Mechanical properties of wire–arc-deposited ATI 718Plus

The true stress–true strain plots of wire–arc-deposited ATI 718Plus deformed at room temperature, under different strain rates, are presented in Fig. 3a. In addition, the

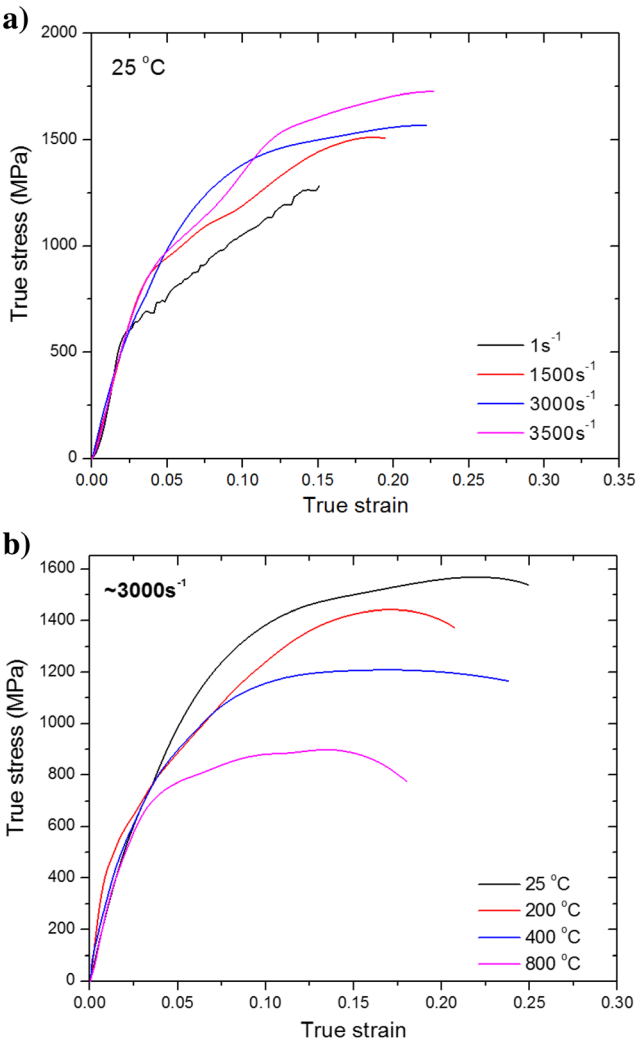

Fig. 3 True stress–true strain of wire–arc-deposited ATI 718Plus (**a**) deformed under various strain rates at room temperature and (**b**) deformed at 3000 s^{-1} at various temperatures

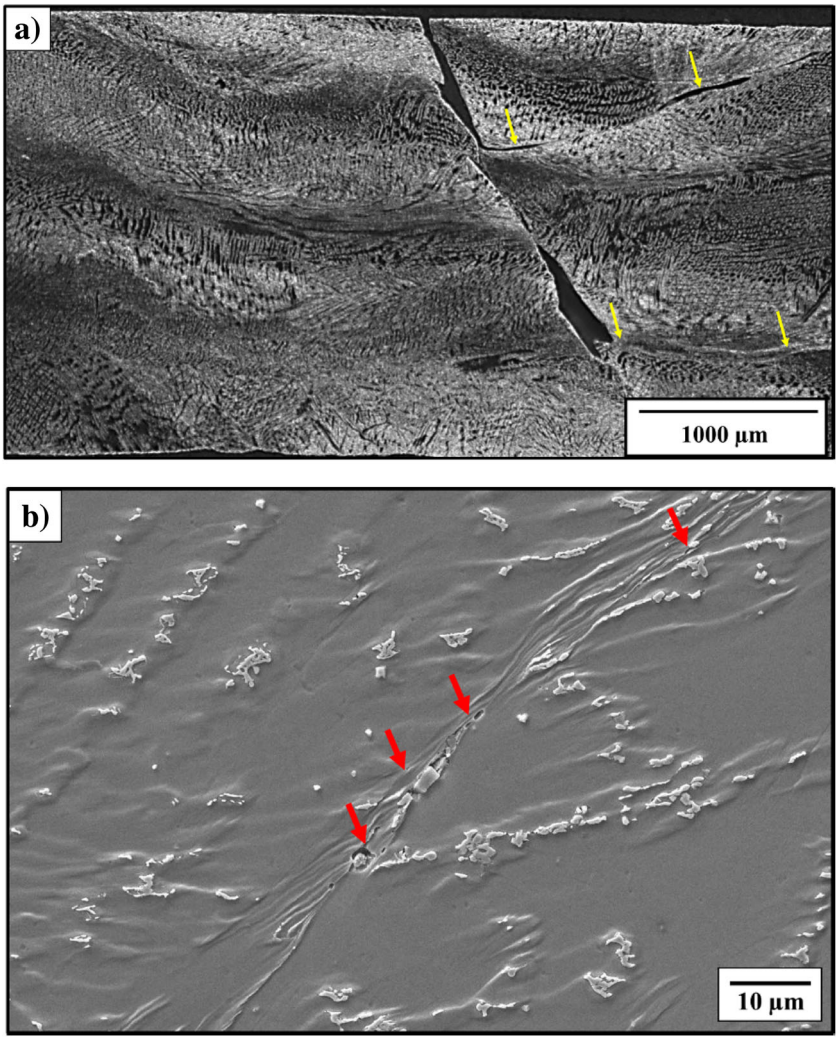

Fig. 4 Post-deformation microstructure of wire–arc-deposited ATI 718Plus showing (**a**) cracking along the clad tracks and (**b**) strain localisation and initiation of cracks at the eutectic constituents

stress–strain plots of the deposit deformed at approximately 3000 s^{-1} under different temperatures are shown in Fig. 3b. It is seen that the flow stress of the deposit is sensitive to both temperature and strain rates. The flow stress of the alloy increases with the increase of the strain rate but decrease with the increase of deformation temperatures.

Representative microstructures of the deposit after deformation, at an approximate strain rate of 3000 s^{-1}, are presented in Fig. 4. The OM image, in Fig. 4a, shows cracking in the deformed alloy, and the crack seems to propagate preferentially along the clad tracks as seen from the yellow arrow. A magnified SEM image in Fig. 4b shows the appearance of localised deformation and the preferential initiation of crack at the secondary solidification constituent. The strain localisation is believed to be promoted by the heterogeneous precipitation of the strengthening phase. The initiation of cracks, within the localised band, is observed to occur at the eutectic constituent and is also believed to be responsible for the propagation of the macro-crack through the test specimen.

3.3 Constitutive models for the flow stress of wire–arc-deposited ATI 718Plus

3.3.1 Arrhenius-type model with compensated strain

It has been shown that the relationship between the temperature, flow stress and strain rates can be expressed by an Arrhenius-type equation [8]:

$$\dot{\varepsilon} = AF(\sigma)\exp\left(\frac{-Q}{RT}\right) \tag{1}$$

$$\text{Where } F(\sigma) = \begin{cases} \sigma^{n'} & \alpha\sigma < 0.8 \\ \exp(\beta\sigma) & \alpha\sigma > 1.2 \\ \sinh(\alpha\sigma)^{n} & \text{for all } \sigma \end{cases}$$

$\dot{\varepsilon}$ is the strain rate (s^{-1}), R is the gas constant (8.314 J/mol^{-1} K^{-1}), Q is the activation energy in kJ/mol and T is the temperature (Kelvin). σ is the flow stress (MPa) for a given strain, and A, β, n' and α are material constants, $\alpha = \beta/n$.

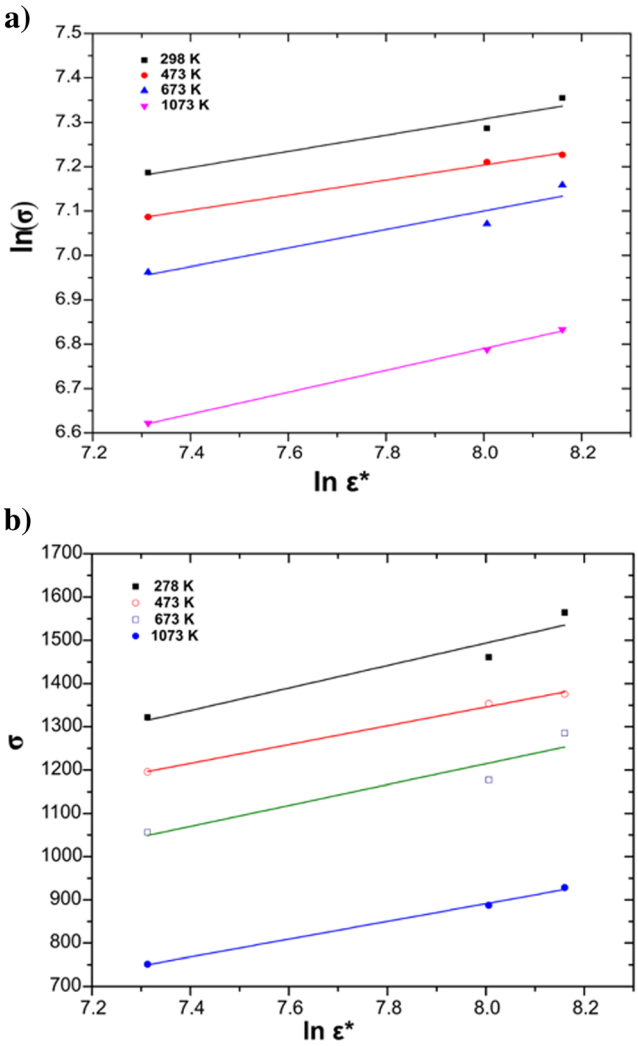

Fig. 5 Plots of (**a**) ln (σ) vs. ln ($\dot{\varepsilon}$) and (**b**) σ vs. ln ($\dot{\varepsilon}$) at 0.075 strain

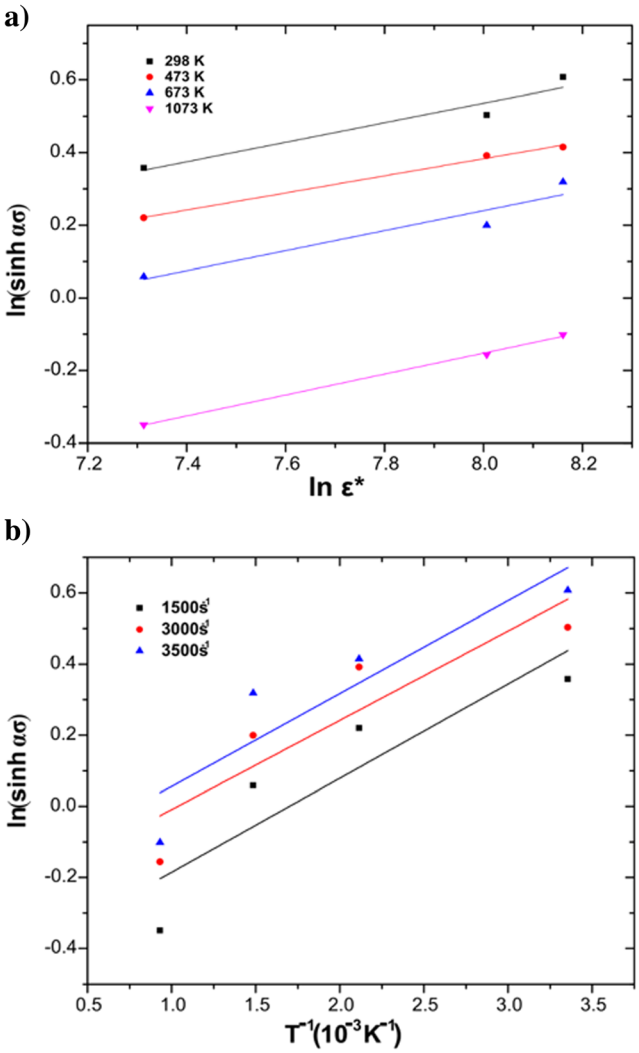

Fig. 6 Plots of (**a**) $\ln[\sinh(\alpha\sigma)]$vs.$\ln(\dot{\varepsilon})$ and (**b**) $\ln\left[\sinh(\alpha\sigma)\text{vs}\frac{1000}{T}\right]$

The Zener–Hollomon parameter (Z) [16] can be used to express the effect of strain rates and temperature on the deformation behaviour of metals and alloys:

$$Z = \dot{\varepsilon}\exp\left(\frac{Q}{RT}\right) \tag{2}$$

The influence of strain on the flow stress of the material is not considered in Eqs. (1) and (2). In this work, a strain-compensated Arrhenius model, as proposed by Lin et al. [19], in which the influence of strain on the material constants is considered. To account for the linear elastic strain, an offset of 0.05 strain is used for the alloys to compensate for the overestimation of the elastic strain during the high strain rate experiments, as seen in Fig. 3a. For illustrating the solution procedure in determining the material constants of the Arrhenius-type model with compensated strain, a plastic strain value of 0.075 is taken as an example.

3.3.2 Estimation of material constants in the Arrhenius-type model

Substituting the power law and exponential law of $F(\sigma)$ into Eq. (1) for the low-stress level ($\alpha\sigma < 0.8$) and high-stress level ($\alpha\sigma > 1.2$), respectively, will yield:

$$\dot{\varepsilon} = B\sigma^{n'} \tag{3}$$

$$\dot{\varepsilon} = B'\exp(\beta\sigma) \tag{4}$$

where B and B' are material constants.

By taking the logarithm of Eqs. (3) and (4), the following are obtained;

$$\ln(\sigma) = \frac{1}{n'}\ln(\dot{\varepsilon}) - \frac{1}{n'}\ln(B) \tag{5}$$

$$\sigma = \frac{1}{\beta}\ln(\dot{\varepsilon}) - \frac{1}{\beta}\ln\left(B'\right) \tag{6}$$

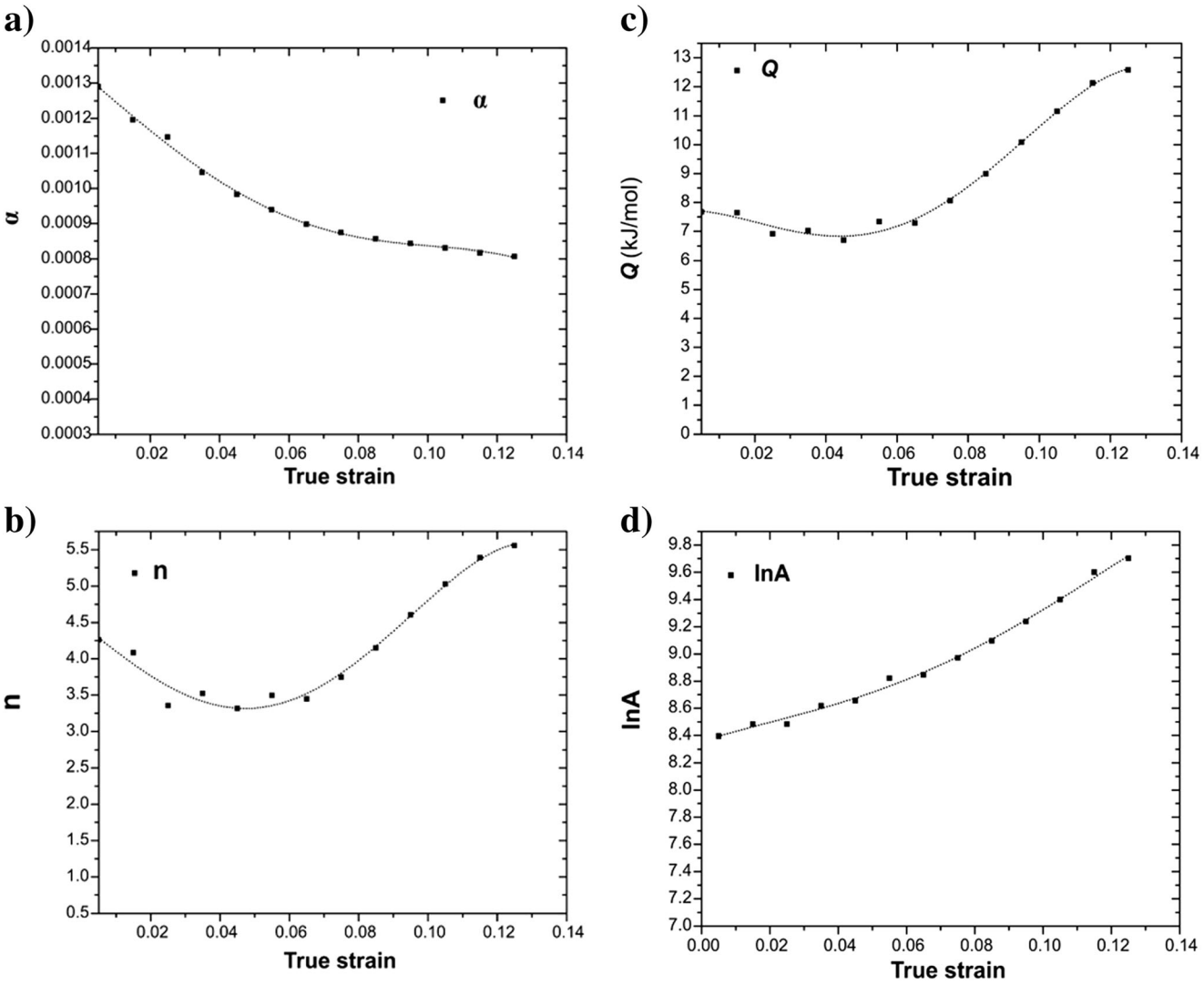

Fig. 7 Variation of material constant (**a**) α, (**b**) n, (**c**) Q and (**d**) lnA

The flow stress values corresponding to the strain rates, from the experiment performed in this work, are substituted into Eqs. (5) and (6), to give the relationship between the flow stress and the strain rates as presented in Fig. 5. The values of n' and β can be obtained from the slope of the plots of ln (σ) vs ln ($\dot{\varepsilon}$) and σ vs ln ($\dot{\varepsilon}$), respectively. The average value of the slopes at different deformation temperatures is used to obtain the values of n' and β, which are subsequently used to compute $\alpha = \beta/n'$. The mean value of n' and β obtained from the plots at 0.075 is 4.43826 and 0.005089, respectively, which produces α, calculated at 0.001146638.

For all stress levels, Eq. (1) can be written as:

$$\dot{\varepsilon} = A\left(\sinh(\alpha\sigma)^n \exp\left(\frac{-Q}{RT}\right)\right) \tag{7}$$

By taking the logarithm of Eq. (7) and rearranging the result yields;

Table 4 Polynomial function coefficient of material constants α, n, Q and ln$A$

α		n		Q		ln$A$	
α_0	0.0013	n_0	4.4708	Q_0	7.71737	D_0	8.3577
α_1	− 0.0082	n_1	− 36.602	Q_1	4.96515	D_1	7.82
α_2	− 0.0203	n_2	− 120.78	Q_2	− 1915.6042	D_2	− 69.347
α_3	0.9784	n_3	10,520	Q_3	37,759.8314	D_3	1390.2
α_4	− 4.4803	n_4	− 53,164	Q_4	− 161,961.3356	D_4	− 5103.1

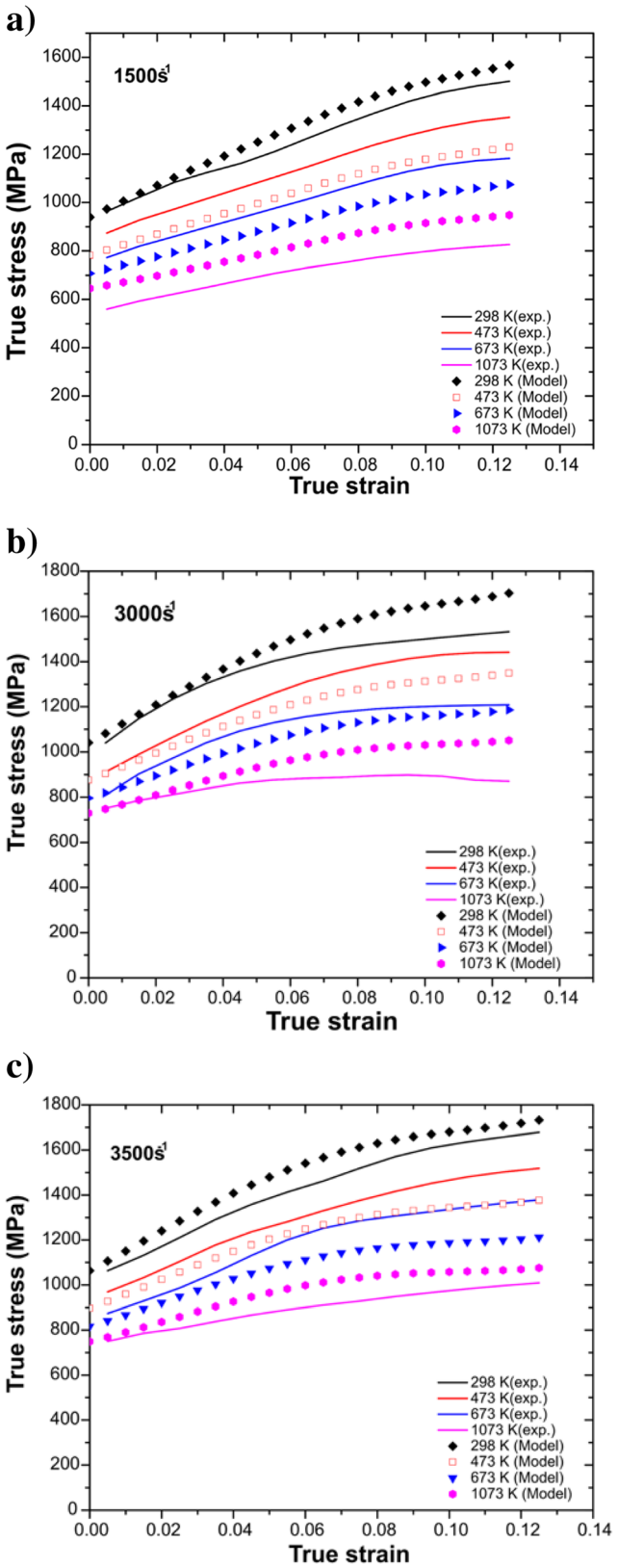

Fig. 8 A plot comparing the experimental flow stress with the predicted values at different strain rates, (**a**) 1500 s^{-1}, (**b**) 3000 s^{-1}, and (**c**) 3500 s^{-1}, using the strain-compensated Arrhenius-type model

$$\ln[\sinh(\alpha\sigma)] = \frac{1}{n}\ln\dot{\varepsilon} + \frac{Q}{nRT} - \frac{lnA}{n} \tag{8}$$

By substituting the values of strain rates and the corresponding flow stress (at 0.075 strain) for all test temperatures into Eq. (8), the relationship between $\ln[\sinh(\alpha\sigma)]$ and $\ln\dot{\varepsilon}$ is plotted in Fig. 6a. The value of n can be obtained from the mean of the slope values from these plots. The differentiation of Eq. (7), at a constant strain rate, gives;

$$Q = Rn\frac{d\left(\ln[\sinh(\alpha\sigma)]\right)}{d(1/T)} \tag{9}$$

The plot of $\ln[\sinh(\alpha\sigma)]$ vs $1000/T$, presented in Fig. 6b, is applied to calculate the activation energy, Q, by using the average of the slope values of the plot at different strain rates. Hence, from the intercept of $\ln[\sinh(\alpha\sigma)]$ vs $\ln(\dot{\varepsilon})$, the value of A can be calculated using Eq. (8).

To compensate for the influence of strain on the flow stress, the values of the material constants (Q, A, n and α) for the constitutive equation are calculated under different strain levels (from 0.005 to 0.125). To express the effect of strain on material constants, a 4th-order polynomial is used to fit each of the constants as presented in Eq. (10) and in Fig. 7. The coefficient of these polynomials is given in Table 4.

$$\begin{aligned} \alpha &= \alpha_0 + \alpha_1\varepsilon^1 + \alpha_2\varepsilon^2 + \alpha_3\varepsilon^3 + \alpha_4\varepsilon^4 \\ n &= n_0 + n_1\varepsilon^1 + n_2\varepsilon^2 + n_3\varepsilon^3 + n_4\varepsilon^4 \\ Q &= Q_0 + Q_1\varepsilon^1 + Q_2\varepsilon^2 + Q_3\varepsilon^3 + Q_4\varepsilon^4 \\ \ln A &= D_0 + D_1\varepsilon^1 + D_2\varepsilon^2 + D_3\varepsilon^3 + D_4\varepsilon^4 \end{aligned} \tag{10}$$

By applying the hyperbolic sine function, the flow stress can be expressed as a function of the Zener–Hollomon parameter, Z (by combining Eqs. (2) and (7)), as presented in Eq. (11):

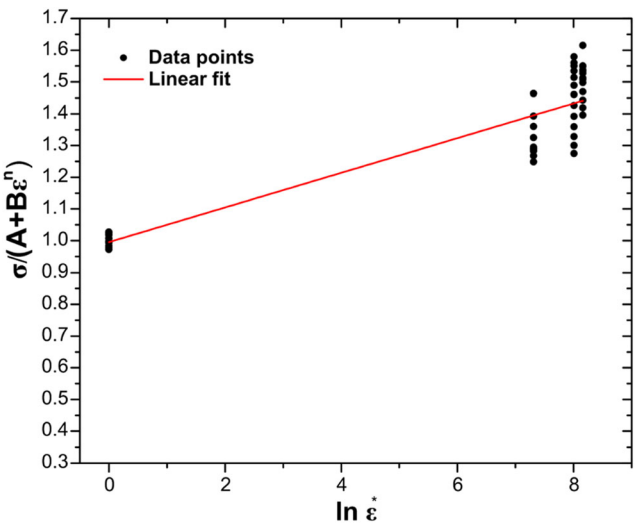

Fig. 9 Plot of $\sigma/(A + B\varepsilon^n)$ against $\ln\dot{\varepsilon}^*$ at reference temperature (293 K)

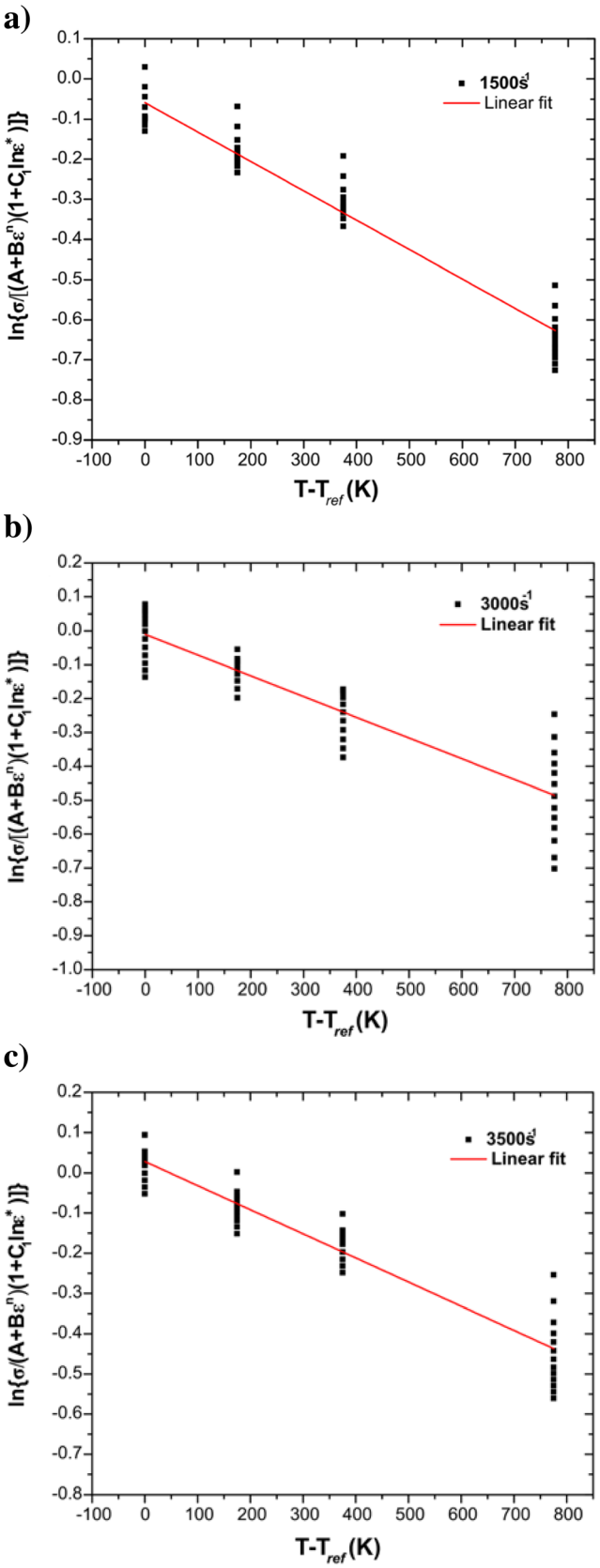

Fig. 10 Plots of $\ln\left\{\sigma/\left[(A+B\varepsilon^{n})\left(1+C_1\ln\dot{\varepsilon}^{*}\right)\right]\right\}$ vs. $(T-T_r)$ at the various strain rates: (**a**) 1500 s^{-1}, (**b**) 3000 s^{-1} and (**c**) 3500 s^{-1}

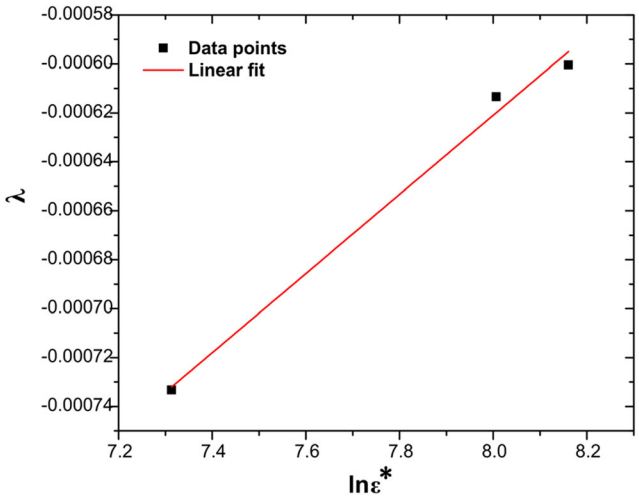

Fig. 11 The plot of and λ against $\ln\dot{\varepsilon}^{*}$

$$\sigma=\frac{1}{\alpha}\ln\left\{\left(\frac{Z}{A}\right)^{\frac{1}{n}}+\left[\left(\frac{Z}{A}\right)^{\frac{2}{n}}+1\right]^{\frac{1}{2}}\right\} \tag{11}$$

Using the strain-compensated Arrhenius equation, a comparison between the predicted flow stress and the experimental data obtained at various strain rates and temperatures is presented in Fig. 8.

3.3.3 Modified Johnson–Cook model

In the present work, a modified Johnson–Cook model which considers the coupled effects of temperature and strain rates on the flow stress while still maintaining the power law in the original J-C model as presented in Eq. (12) is applied:

$$\sigma=(A+B\varepsilon^{n})\left(1+C_1\ln\dot{\varepsilon}^{*}\right)\exp\left[\left(\lambda_1+\lambda_2\ln\dot{\varepsilon}^{*}\right)(T-T_r)\right] \tag{12}$$

where A, B, n, C_1, λ_1 and λ_2 are material constants, ε is the plastic strain, $\dot{\varepsilon}^{*}=\dot{\varepsilon}/\dot{\varepsilon}_0$ is the dimensionless strain rate ($\dot{\varepsilon}$ is the strain rate, while $\dot{\varepsilon}_0$ is the reference strain rate (1 s^{-1})), T is the absolute temperature, T_r (298 K) is the reference temperature and σ is the flow stress. This model applied the strain hardening parts of the original J-C model and the coupled effects of temperature and the strain rate on the flow stress as proposed by Lin et al. [9].

3.3.4 Estimation of the material constants

At the reference temperature (298 K) and strain rate (1 s^{-1}), Eq. (12) is reduced to:

$$\sigma=A+B\varepsilon^{n} \tag{13}$$

The values of A, B and n can be obtained by a non-linear curve fitting and optimisation of the quasi-static experimental σ vs ε data.

Equation (12), at the reference temperature, can be expressed as;

$$\frac{\sigma}{A+B\varepsilon^{n}} = \left(1 + C_1 \ln\dot{\varepsilon}^{*}\right) \tag{14}$$

By substituting the different strain rates and their corresponding flow stress at various strain values into Eq. (14), C_1 can be obtained from the slope of the linear fit of $\sigma/(A + B\varepsilon^{n})$ against $\ln\dot{\varepsilon}^{*}$ as shown in Fig. 9.

Introducing a new parameter λ, where $\lambda = \left(\lambda_1 + \lambda_2 \ln\dot{\varepsilon}^{*}\right)$, Eq. (12) can be expressed as

$$\frac{\sigma}{\left[(A+B\varepsilon^{n})\left(1 + C_1 \ln\dot{\varepsilon}^{*}\right)\right]} = e^{\lambda(T-T_r)} \tag{15}$$

Taking the logarithm of both sides of Eq. (13) yields;

$$\ln\left\{\frac{\sigma}{\left[(A+B\varepsilon^{n})\left(1 + C_1 \ln\dot{\varepsilon}^{*}\right)\right]}\right\} = \lambda(T-T_r) \tag{16}$$

The plots of $\ln\left\{\sigma/\left[(A+B\varepsilon^{n})\left(1 + C_1 \ln\dot{\varepsilon}^{*}\right)\right]\right\}$ vs $(T-T_r)$ are plotted for varying strains and temperatures at different strain rates as presented in Fig. 10. From these plots, λ values are obtained at different strain rates from the slope. The values of λ are plotted against $\ln\dot{\varepsilon}^{*}$, the slope and the intercept, given as λ_2 and λ_1, respectively (seen in Fig. 11). The material constants of the modified Johnson–Cook are summarised in Table 5.

Thus, the relationship among the flow stress (σ), strain (ε), strain rate ($\dot{\varepsilon}$) and temperature (T) is expressed according to the modified Johnson–Cook model in Eq. (17). The plots of flow stress vs true strain using the modified Johnson–Cook are presented in Fig. 12.

$$\boldsymbol{\sigma} = \left(632.5 + 1721.31\varepsilon^{0.655}\right)\left(1 + 0.0658\ln\dot{\varepsilon}^{*}\right)\exp\left[\left(-0.00191 + 1.6172E^{-4}\ln\dot{\varepsilon}^{*}\right)(T-T_r)\right] \tag{17}$$

4 Verification of the constitutive models

The reliability of the constitutive models, the strain-compensated Arrhenius-type and the modified Johnson–Cook models, to predict the flow stress of as-deposited ATI 718Plus was assessed using some standard statistical parameters. The correlation coefficient (R), root-mean-square error (RMSE) and the average absolute relative error (AARE) are the statistical parameters selected and are presented in Eqs. (18), (19), and (20), respectively.

$$R = \frac{\sum_{i=1}^{N}\left(E_i-\overline{E}\right)\left(P_i-\overline{P}\right)}{\sqrt{\sum_{i=1}^{N}\left(E_i-\overline{E}\right)^{2}\sum_{i=1}^{N}\left(P_i-\overline{P}\right)^{2}}} \tag{18}$$

$$RMSE = \sqrt{\frac{\sum_{i=1}^{N}(E_i-P_i)^{2}}{N}} \tag{19}$$

$$AARE\ (\%) = \frac{1}{N}\sum_{i=1}^{N}\left|\frac{E_i-P_i}{E_i}\right| \times 100 \tag{20}$$

where E_i is the experimental data, P_i is the predicted value derived from constitutive models and $\overline{E}$ and $\overline{P}$ are the mean values of E and P, respectively. N is the total number of data points used for the analysis. When the values of $R = 1$, $RMSE = 0$ and $AARE = 0$, the experimental flow stress is perfectly equal to the predicted values of the flow stress by the model. The correlation coefficient usually gives the linear relationship between the obtained experimental data and the predicted values, which can sometimes be prone to bias [23]. In contrast, the average absolute relative error is less biased to the statistical parameter for judging the reliability of a model. They are determined through a term-by-term correlation of the relative error between the predicated value and the experimental data.

The correlation plots between the experimental data and predicted values are presented in Fig. 13. In addition, the values of R and $AARE$ calculated from the data using both the strain-compensated Arrhenius-type model and the

Table 5 Evaluated Johnson–Cook material constant

J-C material constant	A	B	n	C_1	λ_1	λ_2
Value	632.5	1721.31	0.655	0.0658	− 0.00191	1.6173×10^{-4}

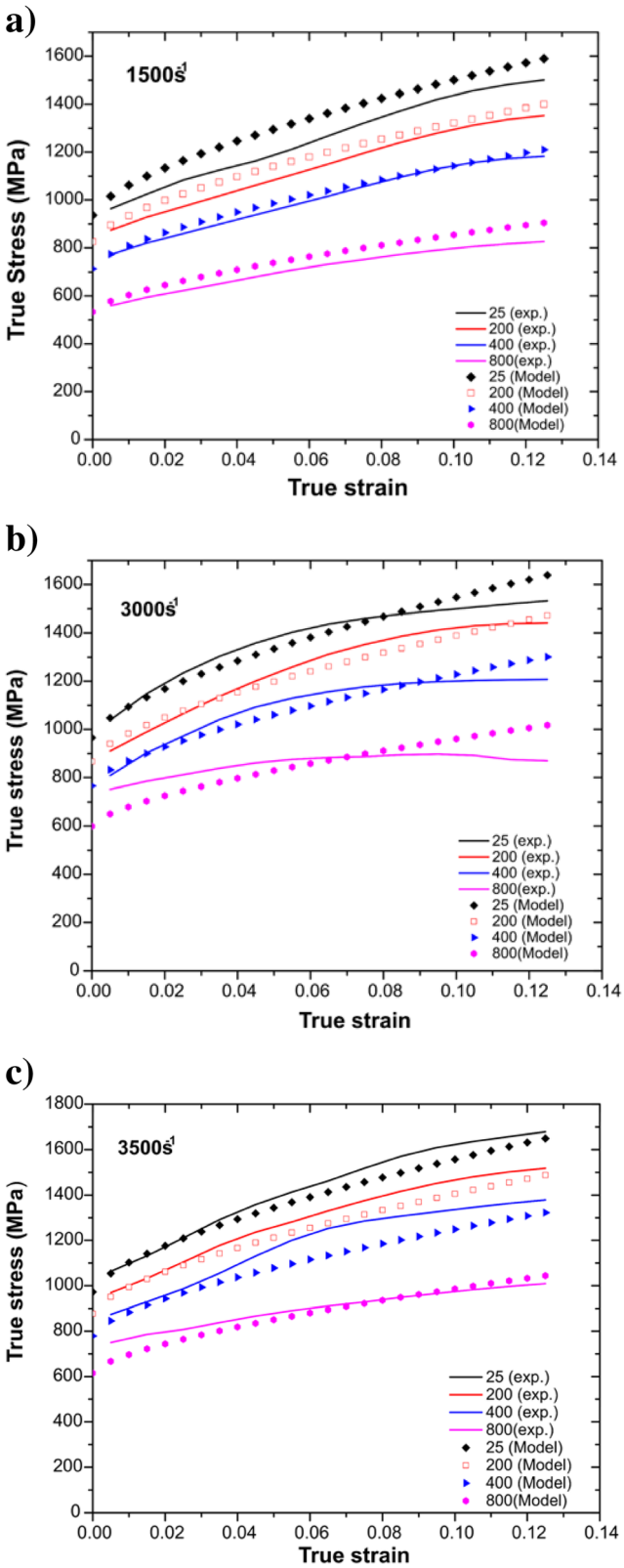

Fig. 12 Plots comparing the flow stress from experimental data and predicted values using the modified Johnson–Cook model at various strain rates, (**a**) 1500 s^{-1}, (**b**) 3000 s^{-1} and (**c**) 3500 s^{-1}

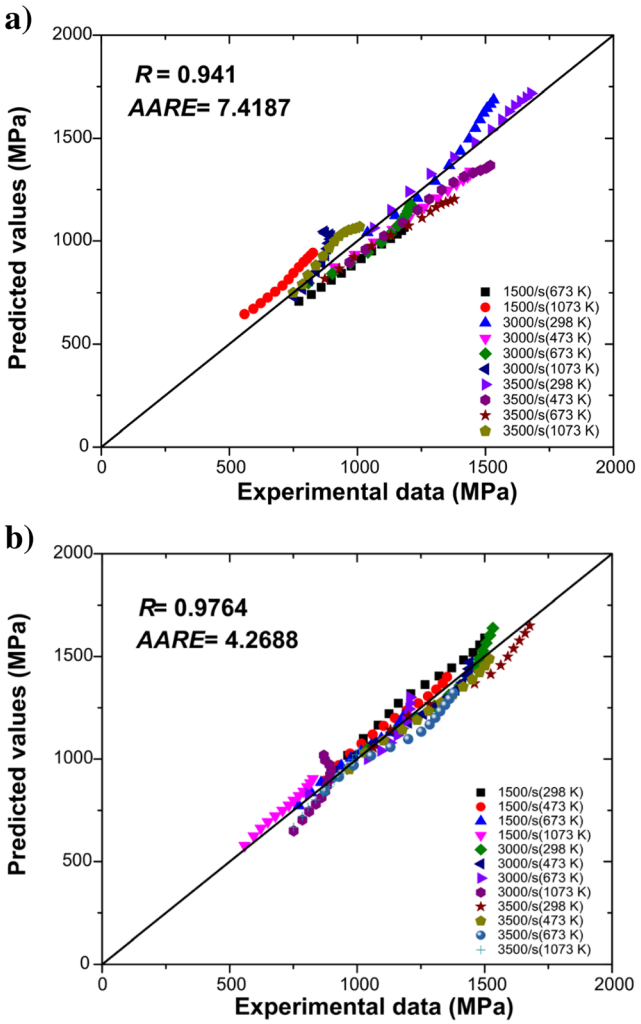

Fig. 13 Correlation between experimental data and the predicted flow stress using (**a**) strain-compensated Arrhenius-type model and (**b**) modified Johnson–Cook model

modified Johnson–Cook model are embedded in the respective correlation plots. The modified Johnson–Cook model produces a higher correlation coefficient and a lower value for the AARE, in comparison to the strain-compensated Arrhenius-type model. In addition, the RMSE in Fig. 14a shows a general higher value for the Arrhenius-type model in comparison to the modified Johnson–Cook model. This demonstrates that the modified Johnson–Cook model is a more suitable constitutive model to predict the flow stress of as-processed ATI 718Plus superalloy under high strain rate deformation.

The higher predictability of the modified Johnson–Cook model may be attributed to the ability to better model the coupled effects of temperature and strain rates on the flow stress of the deposit. The λ_1 and λ_2 in the term $\left(\exp\left[\left(\lambda_1+\lambda_2\ln\dot{\varepsilon}^{*}\right)(T-T_r)\right]\right)$ of the modified Johnson–Cook model represent the coupled effect of temperature and strain rate and thus have a better predictability. In the strain-

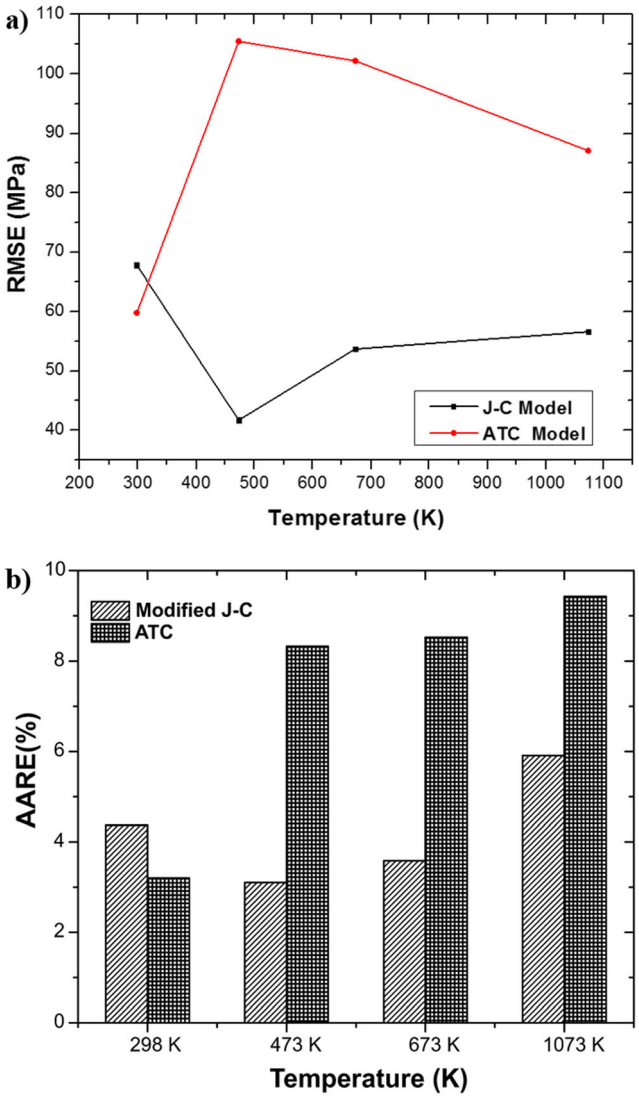

Fig. 14 AARE plot against the deformation temperature for the modified J-C and ATC models

compensated Arrhenius-type model, however, the coupled effects of temperature and strain rate are represented by the material constant, Q. To obtain Q, a linear fit is assumed for the plot of ln[sinh($\alpha\sigma$)vs 1000/T] at a given strain, it can, however, be observed from Fig. 6b that the linear fit provides a poor fit for the plot for all strain rates. The linear fit underestimates the stress at 473 and 673 K but overestimated the stress at high temperature (1073 K) as seen in Fig. 6b. The temperature dependence on the flow stress of deposited ATI 718Plus is predominately dictated by the intermetallic strengthening precipitate, γ'. In this alloy, the strengthening effect of γ' precipitates is effective up to moderately high temperatures, ~ 973 K [24], accompanied with a little decrease in strength. At higher temperatures, however, a sharp drop in strength is usually observed as evident at 1073 K in Fig. 6b, and the non-linearity of ln[sin$h$($\alpha\sigma$)vs 1000/T] (from 298 to 1073 K) may be attributable to this phenomenon. As a result of the inaccuracy from the estimation of the material constant, Q, the predictability of the strain-compensated Arrhenius model is negatively affected at those temperatures (as seen in the *RMSE* and *AARE* vs deformation temperature plots in Fig. 14). It can be observed that at the reference temperature (298 K), the strain-compensated Arrhenius model shows a low value of RMSE and AARE, however, the error increases significantly at high deformation temperature. The error in the modified JC model remains low and moderately varies over the all deformation temperatures.

5 Conclusion

The high strain rate deformation of the as-deposited ATI 718Plus superalloy was characterised at a range of temperatures and strain rates using the direct-impact Hopkinson pressure bar. Results from the experiment show that the deformation behaviours of WAAM ATI 718Plus, in the as-deposited condition, are affected by the deformation temperature, strain and strain rates. Based on the experimental data, constitutive models, based on strain-compensated Arrhenius-type and modified Johnson–Cook models, were applied to describe the flow stress of the deposit. Comparing the predictability of the two constitutive models, the modified Johnson–Cook model showed a greater accuracy as compared to the Arrhenius-type model with compensated strain. A higher correlation coefficient ($R = 0.9828$) was observed for the modified Johnson–Cook model with a relatively lower average absolute relative error ($AARE = 4.387187$) in comparison to the strain-compensated Arrhenius model with $R = 0.94067$ and $AARE = 7.4187$. The poor predictability of strain-compensated Arrhenius model can be attributed to the models' inability to accurately capture the effect of temperature on the flow stress of the precipitation-strengthened ATI 718Plus deposit.

Acknowledgments Financial support from the Natural Sciences and Engineering Research Council of Canada is gratefully acknowledged. One of the authors (Gbenga Asala) also acknowledges the award of the University of Manitoba Graduate Fellowship during his Ph.D. programme.

References

1. Cao WD, Kennedy RL (2004) Role of chemistry in 718 type alloys—Allvac® 718Plus™ development. Superalloys 2004. TMS (The Minerals, Metals & Materials Society), Seven Springs
2. Jeniski RA Jr, Kennedy RL (2006) Development of ATI Allvac® 718Plus® alloy and applications. Symposium on recent advantages of Nb-contain materials in Europe
3. English CL, Tewari SK, Abbott DH (2010) An overview of Ni base additive fabrication technologies for aerospace applications. In: 7th

International Symposium on Superalloy 718 and Derivative. TMS, Pittsburgh, PA
4. Williams SW, Martina F, Addison AC, Ding J, Pardal G, Colegrove P (2015) Wire+arc additive manufacturing. Mater Sci Technol 032: 641–647
5. Arrazola PJ, Özel T, Umbrello D, Davies M, Jawahir IS (2013) Recent advances in modelling of metal machining processes. CIRP Ann Manuf Technol 62:695–718
6. Jafarian F, Imaz Ciaran M, Umbrello D, Arrazola PJ, Filice L, Amirabadi H (2014) Finite element simulation of machining Inconel 718 alloy including microstructure changes
7. Johnson GR, Cook WH (1985) Fracture characteristics of three metals subjected to various strains, strain rates, temperature and pressure. Eng Fract Mech 21:31–45
8. Sellars C, McTegart WJ (1966) On the mechanism of hot deformation. Acta Metall 14:1136–1138
9. Lin YC, Chen X-M, Liu G (2010) A modified Johnson-Cook model for tensile behaviors of typical high-strength alloy steel. Mater Sci Eng A 527:6980–6986
10. Wang X, Huang C, Zou B, Liu H, Zhu H, Wang J (2013) Dynamic behavior and a modified Johnson–Cook constitutive model of Inconel 718 at high strain rate and elevated temperature. Mater Sci Eng A 580:385–390
11. Zhao Y, Sun J, Li J, Yan Y, Wang P (2014) A comparative study on Johnson-Cook and modified Johnson-Cook constitutive material model to predict the dynamic behavior laser additive manufacturing FeCr alloy
12. Couque H, Boulanger R, Bornet F (2006) A modified Johnson-Cook model for strain rates ranging from 10^{-3} to 10^{5} s^{-1}. J Phys IV France 134:87–93
13. He A, Xie G, Zhang H, Wang X (2013) A comparative study on Johnson-Cook, modified Johnson-Cook and Arrhenius-type constitutive models to predict the high temperature flow stress in 20CrMo alloy steel. Mater Des 52:677–685
14. Xue J, Zhang A, Li Y, Qian D, Wan J, Qi B, Tamura N, Song Z, Chen K (2015) A synchrotron study of microstructure gradient in laser additively formed epitaxial Ni-based superalloy. Sci Rep 5: 14903
15. Zhang D-N, Shangguan Q-Q, Xie C-J, Liu F (2015) A modified Johnson-Cook model of dynamic tensile behaviors for 7075-T6 aluminum alloy
16. Zener C, Hollomon JH (1944) Effect of strain rate upon plastic flow of steel. J Appl Phys 15:69
17. Slooff FA, Zhou AJ, Duszczyk AJ, Katgerman AL (2008) Strain-dependent constitutive analysis of three wrought Mg-Al-Zn alloys
18. Slooff FA, Zhou J, Duszczyk J, Katgerman L (2007) Constitutive analysis of wrought magnesium alloy Mg-Al4-Zn1. Scr Mater 57: 759–762
19. Lin YC, Chen M-S, Zhong J (2007) Constitutive modeling for elevated temperature flow behavior of 42CrMo steel. Comput Mater Sci 42:470–477
20. Asala G, Andersson J, Ojo OA (2018) A study of the dynamic impact behaviour of IN 718 and ATI 718Plus® superalloys. Philos Mag 1–19
21. Asala G, Andersson J, Ojo OA (2018) Improved dynamic impact behaviour of wire-arc additive manufactured ATI 718Plus. Mater Sci Eng A. In Press
22. Asala G, Khan AK, Andersson J, Ojo OA (2017) Microstructural analyses of ATI 718Plus? Produced by wire-arc additive manufacturing process. Metall Mater Trans A 48:4211–4228
23. Trimble D, Shipley H, Lea L, Jardine A, O'Donnell GE (2016) Constitutive analysis of biomedical grade Co-27Cr-5Mo alloy at high strain rates. Mater Sci Eng A. 682:466–474
24. Kennedy RL (2005) Allvac ® 718Plus™, superalloy for the next forty years. Superalloys 718, 625, 706 and derivatives. TMS, Pittsburgh